Space Weather

RESEARCH ARTICLE
10.1029/2019SW002166

Incorporation of Heliospheric Imagery Into the CME Analysis Tool for Improvement of CME Forecasting

S. J. Wharton[1,3], G. H. Millward[2], S. Bingham[1], E. M. Henley[1], S. Gonzi[1], and D. R. Jackson[1]

[1]The Met Office, Exeter, UK, [2]National Oceanic and Atmospheric Administration, Boulder, CO, USA, [3]Department of Physics and Astronomy, University of Leicester, Leicester, UK

Key Points:
- We developed a new CME analysis tool called CAT-HI that incorporates Heliospheric Imagery from the STEREO spacecraft
- CAT-HI could enable ensemble pruning when running ensemble forecasts for CMEs and trajectory corrections
- CAT-HI could also be used in conjunction with a dedicated mission to L4 or L5

Correspondence to:
S. J. Wharton,
sjw136@le.ac.uk

Citation:
Wharton, S. J., Millward, G. H., Bingham, S., Henley, E. M., Gonzi, S., & Jackson, D. R. (2019), Incorporation of Heliospheric Imagery into the CME Analysis Tool for improvement of CME forecasting. *Space Weather*, *17*, 1312–1328. https://doi.org/10.1029/2019SW002166

Received 21 JAN 2019
Accepted 2 JUL 2019
Accepted article online 9 JUL 2019
Published online 24 AUG 2019

Abstract Coronal mass ejections (CMEs) cause the largest geomagnetic disturbances at Earth, which impact satellites, wired communication systems, and power grids. The CME Analysis Tool (CAT) is used to determine a CME's initial longitude, latitude, angular width, and radial speed from coronagraph images. These are the initial conditions for the Wang-Sheeley-Arge Enlil solar wind model, along with the ambient solar wind properties derived from magnetograms. However, the coronagraph imagery is limited by field of view. We have incorporated heliospheric imagery (HI) from the Solar Terrestrial Relations Observatory into CAT to create the CME Analysis Tool with Heliospheric Imagery (CAT-HI). These HI images have a larger field of view, allowing tracking of CMEs to greater distances from the Sun. We have compared the performances of CAT and CAT-HI by examining the expected arrival times of CMEs at the L1 Lagrange point and found them to be consistent. However, CAT-HI is advantageous because it could be used to prune ensemble forecasts and issue routine updates for CME arrival time forecasts. Finally, we discuss CAT-HI in the context of an operational mission at the L4 or L5 Lagrange points.

Plain Language Summary Our Sun often releases large explosions of hot charged particles. These eruptions can travel through space all the way to the Earth. Here, they can damage satellites and disrupt communication systems and power grids. Therefore, we would like to predict their arrival time accurately, but currently, this is difficult. At the moment, operators use a tool based on coronagraph images, which look at the atmosphere of the Sun. This allows them to see the eruptions leaving the Sun. However, coronagraphs have a limited field of view, so the operators quickly lose sight of the eruptions. In this work, we have added a new kind of imagery that directly images the eruptions in the space between the Sun and the Earth. This new tool will allow the operators to track the eruptions for longer and to update their predictions of when they will arrive at Earth. The new tool could also be used in conjunction with a dedicated operational mission to monitor these eruptions. In summary, we think that the new tool presented in this paper could be a major advance in our ability to forecast these violent ejections.

1. Introduction

Coronal mass ejections (CMEs) are of the utmost importance in predicting geoeffective space weather events. In September 2017, active region AR12673 released three CMEs within the space of a week, along with 4 X-class solar flares and a Solar Energetic Particle event that caused a ground level enhancement (Redmon et al., 2018). These space weather effects can endanger technology and human lives. During the 2017 hurricane season, these solar flares caused a radiation blackout that impacted disaster relief efforts, and the CMEs compressed the magnetosphere sufficiently to put geosynchronous satellites in the magnetosheath. This was a rare case of intense space weather coinciding with extreme terrestrial weather. Redmon et al. (2018) provide a full account of this incident and its consequences. This event underlines the importance of accurate CME forecasting, the focus of this paper. CMEs are also responsible for creating geomagnetically induced currents, due to the way they compress the magnetosphere (Pulkkinen et al., 2017; Sibley et al., 2012). This can be damaging to electric power grids and wired communications systems.

Multiple methods have been proposed to fit CME fronts for the purposes of determining their speed. For example, these include the fixed-Φ method (Rouillard et al., 2008) and the harmonic mean method (Lugaz, 2010). Lugaz et al. (2012) compared these two methods and found that the harmonic mean method gave a more accurate time of arrival. Colaninno et al. (2013) compared six ways of fitting the CME leading edge and compared the time of arrivals of each. Howard and Tappin (2010) use their own model that accounts for

the appearance of the CMEs in the images. All of these studies used heliospheric imager (HI) data from the Solar Terrestrial Relations Observatory (STEREO; Driesman et al., 2008, Howard et al., 2008, Kaiser et al., 2008). These are white light images of CMEs and are explained more below. This study develops the CME Analysis Tool (CAT) developed by Millward et al. (2013) to fit the CME's leading edge visually.

Currently, the CAT is used for operational space weather forecasting at the National Oceanic and Atmospheric Administration Space Weather Prediction Center (SWPC) in the United States and the Met Office Space Weather Operations Centre (MOSWOC) in the United Kingdom. The goal of CAT is to determine the initial parameters of a CME at 21.5 solar radii. This is the inner boundary of the Enlil solar wind model (Odstrčil & Pizzo, 1999; Odstrčil et al., 2002; Odstrčil, 2003), which can be used to estimate the time of arrival of the CME at Earth. These parameters are the latitude, longitude, angular width, and radial speed of the CME. For operations, the CAT uses beacon-quality coronagraph images of CMEs, ideally from at least three spacecraft. From 2006 to 2014, these were the Large Angle Spectroscopic Coronograph (LASCO; Brueckner et al., 1995) C2 and C3 coronagraphs on the Solar and Heliospheric Observatory (SOHO; Domingo et al., 1995) and the COR2 coronagraphs on the STEREO A (Ahead) and B (Behind) satellites. However, since 2014, contact has been lost with STEREO B, so only SOHO and STEREO A are currently in use operationally (https://stereo-ssc.nascom.nasa.gov/behind&urluscore;status.shtml). Henceforth, we will only discuss the two-satellite case. Many scientific studies have used the CAT to investigate CMEs (e.g., Cash et al., 2015; Lee et al., 2015), albeit using science-quality images. Science-quality images are preferable to beacon-quality images due to better temporal coverage and improved detail. However, they are not available in near real time. This study uses science-quality images.

The CAT works by projecting a three-dimensional lemniscate (teardrop shape) on to the CME in corresponding two-dimensional coronagraph images from the two satellites. These images do not have to occur at simultaneous times. The lemniscate was an improvement on the simpler cone model of Xie et al. (2004). This model suffered from a degeneracy between the half angle and radius of the cone for halo CMEs and systematically underestimated the speed of the CMEs (de Koning et al., 2012). Using the CAT, the operator can adjust the latitude, longitude, half angle, and radius of the lemniscate to "lasso" the front edge of the CME as it appears in the two images. This fitting is done visually by the operator. The radius of the lemniscate can then be changed for subsequent images to produce a CME leading edge versus time plot from which the radial velocity of the CME can be calculated.

Two important assumptions of the CAT are that the initially defined latitude, longitude, and half angle remain constant and that the CME does not accelerate. Another assumption is that the CME has a circular front. Use of the CAT depends on the skill of the human forecaster, which means the fitting process is subjective and depends on their personal definition of where the CME leading edge is located. Allowing the latitude, longitude, and half angle to vary would increase the number of degrees of freedom the operator has to manage when fitting the lemniscate. Using an elliptical lemniscate would introduce a further three degrees of freedom (major axis, minor axis, and rotation). This would make the fitting intractable. Therefore, the assumptions of a constant, radially expanding, circular shape are used to reduce the complexity for forecasters when using the tool.

These three parameters, plus the radial velocity estimate, can then be used to create a "cone file." The density of the CME used in the cone file is assumed to be four times greater than the background density. Changing the density is expected to impact the CME arrival time, but currently, we have no way to measure it, so this is the assumption employed. This cone file can be put into the Enlil solar wind model to understand how the CMEs propagate toward Earth. Also required is the background solar wind speed, which is calculated using the Wang-Sheeley-Arge (WSA) model (Arge & Pizzo, 2000; Arge et al., 2003; Arge et al., 2004; Sheeley, 2017; Wang & Sheeley, 1990). This model uses magnetograms from the Global Oscillations Network Group (Hill, 2018) to calculate the solar wind velocity. These two models are then combined to form WSA-Enlil. WSA-Enlil is in use operationally at both SWPC (Parsons et al., 2011) and MOSWOC and is used to model the propagation of CMEs throughout the solar system.

Currently, the operational imagery is limited by the fields of view of the COR2 and LASCO C3 coronagraphs on STEREO A and SOHO, respectively. These are 15 and 32 solar radii, respectively. Therefore, using CAT, we can only observe the CME from one viewpoint at 21.5 solar radii. It is at this distance that multiple viewpoints are most necessary. By contrast, the wider fields of view of the STEREO heliospheric imagers (HI-1 and HI-2) provide the opportunity to directly image the CMEs as they propagate through the heliosphere all the

way to the Earth. This cannot be done with coronagraphs. For example, HI-1 has a field of view from around 15 solar radii to over 80 solar radii. Hence, it is clear that using HI-1 data can address the issue of a lack of coronagraph data at 21.5 solar radii. Both heliospheric imagers work by detecting Thomson scattered white light from the charged particles in the CME.

Accordingly, we have updated the CAT tool to include science-quality heliospheric imagery (Eyles et al., 2009) from the STEREO A satellite and hence created the CME Analysis Tool with Heliospheric Imagery (CAT-HI). CAT-HI uses a more complex viewing geometry than CAT did. It uses a "camera object" in order to project the lemniscate onto the HI images, which are assumed to be flat - an assumption discussed further in section 2.1 and the appendix where we find it is reasonable to treat the HI-1 images as flat. Estimating the CME speed using measurements extending to a greater distance from the Sun will also improve the linear velocity estimation at 21.5 solar radii. The studies previously mentioned by Howard and Tappin (2010), Lugaz et al. (2012), and Colaninno et al. (2013) all employed HI data. Harrison et al. (2017) have already argued that HI can be used to improve space weather forecasting, and Amerstorfer et al. (2018) have performed ensemble runs on CMEs using the HI data.

In this paper, we compare CAT-HI to the operational CAT. We assess the consistency of the tool in initial parameter selection, the difference in field of view, and predicted CME arrival times. Finally, we discuss how CAT-HI could be used in conjunction with ensemble modeling of CMEs to prune ensembles, how it could be used to provide CME trajectory corrections, and its relevance to a hypothetical operational mission at the L4 or L5 Lagrange point.

2. CAT-HI: CME Analysis Tool with Heliospheric Imagery

2.1. Additional Features for CAT-HI

Since the loss of STEREO B, the CAT has relied only on images from SOHO and STEREO A. To reflect this in CAT-HI, we have removed the STEREO B panel so only two image panels remain, which can be seen in Figures 1 and 2 at the top. These can be compared to a similar screenshot in Millward et al. (2013) of the original three-panel CAT. For operational usage, the CAT uses beacon-quality coronagraph data from STEREO. These files have a greater compression and poorer resolution than science-quality images but are available to the forecasters in near real time. In a similar manner, CAT-HI can show beacon- and science-quality HI-1 images, which are shown in Figures 1 and 2, respectively, so the reader can see the difference. Science and beacon images are different images taken at different times, hence the mismatch of ~1 hr between the timestamps in Figures 1 and 2 for both HI-1 and LASCO C3 images. The difference in appearance can also be due to differences in the image properties (e.g., image saturation). Despite both figures showing the same CME at approximately the same time, the shape of the manually fitted lemniscate is different. This is mainly because it is difficult to replicate the CAT tool operator's subjective judgment of where the CME's leading edge is on different fits of the same set of images, rather than because of the differences in quality between the beacon and science images. This subjectivity is one of the limitations of the tool. We used science-quality data for this study as the CAT-HI tool was initially developed for STEREO science-quality imagery, the rationale being that a future L4/L5 mission would likely aim to provide the equivalent of STEREO's science-quality imagery on an operational basis. Nevertheless, Figure 1 shows that it is also possible to use STEREO's beacon-grade imagery in CAT-HI. Hence, its usefulness is not contingent on having science-grade imagery from any future mission. Science-quality images are also taken more frequently by the HI cameras, giving better coverage of CME events for our study.

Another complication is that because STEREO A has passed solar conjunction, it is now behind the Earth in its orbit. Originally, an earthward-directed CME would propagate left across the STEREO A image toward the middle panel (SOHO image) and propagate right across the STEREO B image, also toward the middle panel. But because STEREO A is now behind the Earth in its orbit, earthward-directed CMEs propagate the opposite way across the image, away from the middle panel. The position of the two panels (after removal of STEREO B) was discussed with the MOSWOC forecasters, and, for consistency, we have left the STEREO A panel on the right.

Another small change is that the animation panel, which allowed the user to animate a series of images, has now been removed after conversation with the MOSWOC forecasters. It was agreed this was not a useful feature, so all aspects of it have been removed.

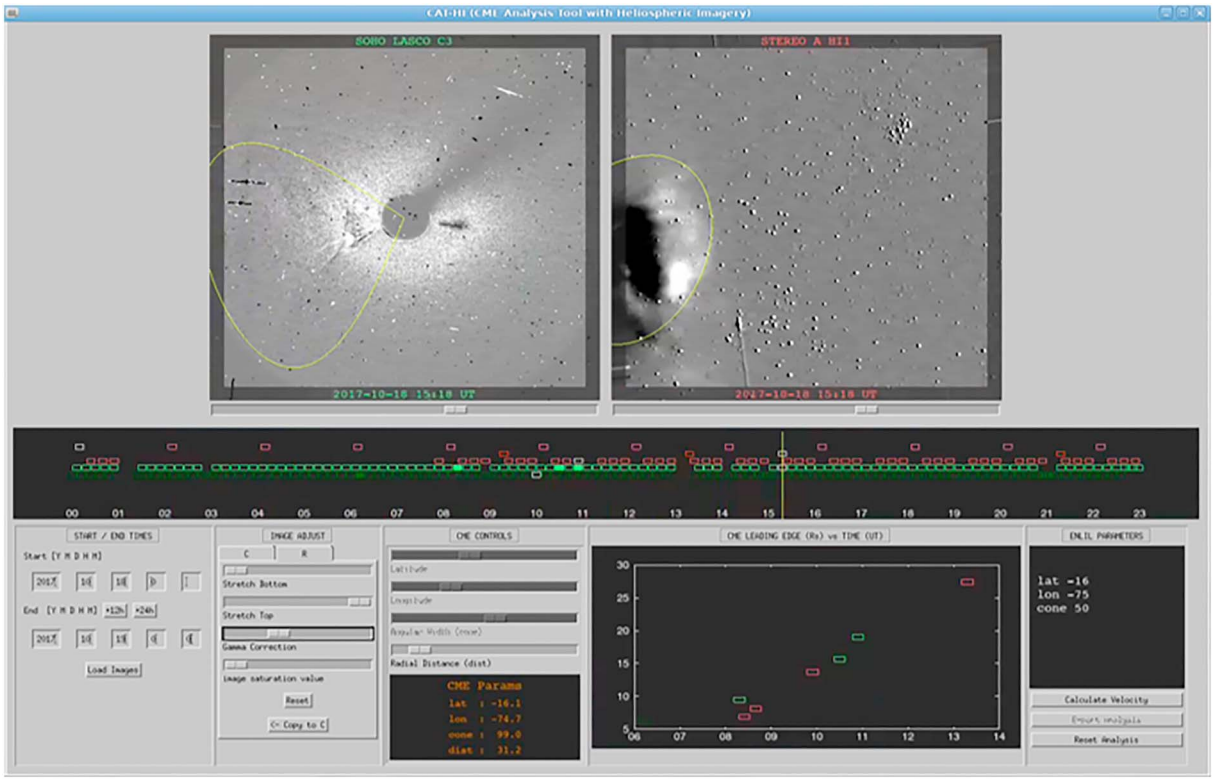

Figure 1. Cropped screenshot of the new interface for CAT-HI. The top left panel shows images from the SOHO LASCO C2 or C3 coronagraphs. The top right panel shows images from either the COR2 coronagraph, HI-1 telescope, or HI-2 telescope on the STEREO A spacecraft. This figure shows beacon-quality HI-1 data on the right. Below is the imagery timeline, where each rectangle represents an image's universal time. Spaces represent data gaps, but these can be backfilled later if the images become available—a common occurrence in operational use. Filled in rectangles indicate which images have been used to create the range-time plot. In the bottom row, from left to right, are panels to load the images, adjust their properties (such as image saturation), sliders to determine the lemniscate properties, the plot to show leading edge of the CME versus time and the controls to determine the velocity and save the CME metadata.

The main change is the introduction of HI-1 and HI-2 imagery from STEREO A. L1 DNS (data numbers per second per CCD pixel) images were downloaded from the U.K. Solar System Data Centre (https://www.ukssdc.ac.uk/solar/). The HI-1 and HI-2 images are treated equivalently to the coronagraph images; that is, as flat squares—they are not projected onto the inside of a sphere. This is a reasonable assumption for HI-1, which has a smaller field of view, but unreasonable for HI-2. This assumption is discussed in Appendix A. Hence, we only use HI-1 data in this proof-of-concept study.

Forecasters now have the option to switch the image source on the right-hand panel between COR2, HI-1, and HI-2. The black imagery timeline in the middle has been updated to accommodate this and the lemniscate scaling updated to fit the fields of view of the two HI telescopes. An example of the lemniscate *lassoing* a CME in HI-1 data is shown in the top right panel of Figures 1 and 2. At this point in the process, the CME has evolved far from the images at which its latitude, longitude, and angular width were defined. This means the fit looks more ambiguous and the CMEs are fainter than in early images due to their spatial dissipation. However, we have chosen this image to showcase the propagation of the CME's radial position with time in the graph in the bottom row. It is from this graph that the radial velocity of the CME is calculated.

2.2. Validation of CAT-HI Against the Operational CAT

CAT and CAT-HI were used (by the first author) to analyze the properties of 13 CMEs selected from the Goddard Space Flight Centre LASCO CME catalogue (https://cdaw.gsfc.nasa.gov/CME&urluscore;list/). CMEs were identified from January 2016 to October 2017 that met the following criteria: (1) were not classed as poor or very poor in the remarks column, (2) were classed as Halo in the Central PA [deg] column, and (3) were clearly visible to us when loaded into the CAT tool. This gave 13 CME events across the 22 months, including the three CMEs described in Redmon et al. (2018). During this time, STEREO A was located between −164° and −132° Earth ecliptic longitude so would be viewing earthward CMEs from the rear. These nonideal angles will reduce the accuracy of the lemniscate fitting.

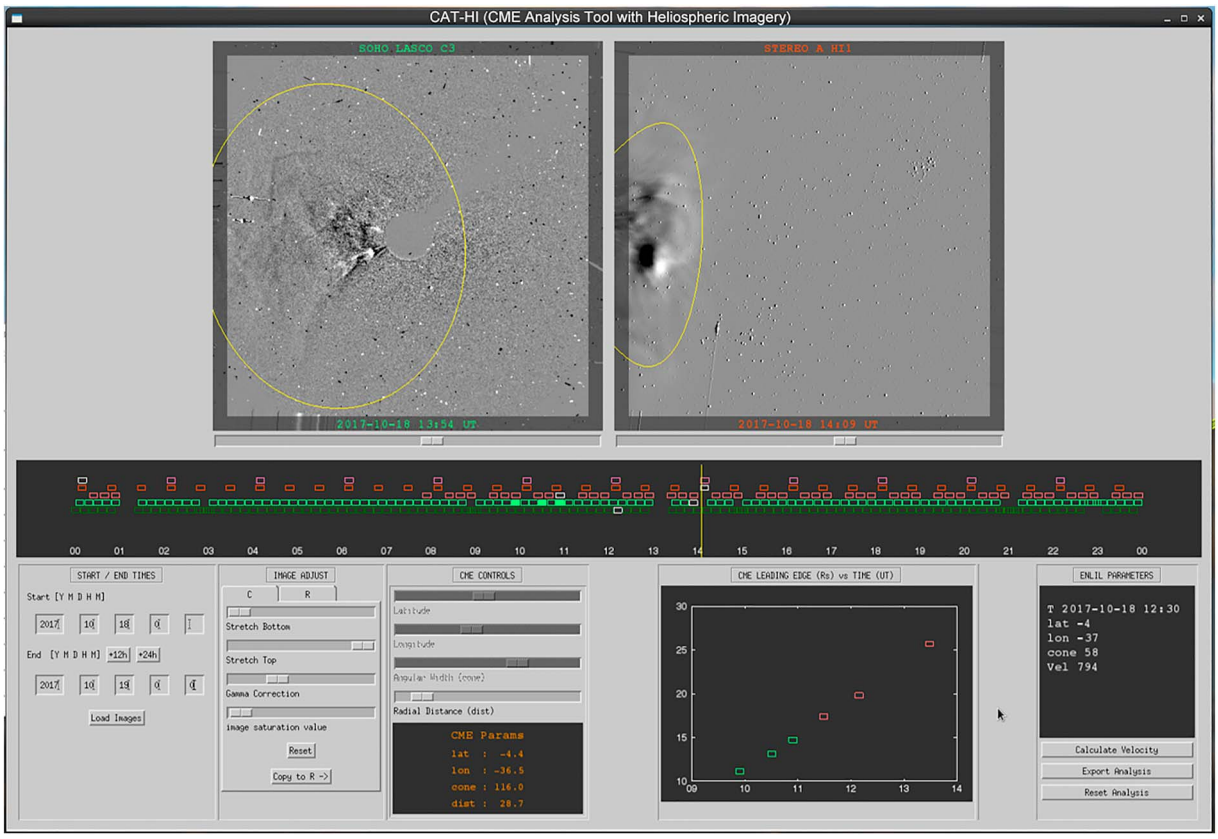

Figure 2. This screenshot shows the same CAT-HI interface as Figure 1 but with science-quality HI-1 data. Note that the science-quality HI-1 images were taken at different times, hence the different timeline.

These CMEs were first analyzed with CAT then CAT-HI. There was no randomization or blinding, which was considered acceptable as these methods would have been ineffective for the small sample size. The images analyzed were running differences, where the previous image was subtracted from the current. This made it easier to observe the CME. The latitude, longitude, and half angle of the CME/lemniscate were fixed using a single pair of images, usually from LASCO C3 and COR2. The fit of the lemniscate to the image was entirely visual. The radius of the lemniscate was then varied for subsequent and previous sets of images and a linear fit used to determine the radial velocity. For fitting the lemniscate in HI images using CAT-HI, the initial parameters from the COR2 images were kept for use on the HI images. The fit of the lemniscate to the CME was observed to worsen as the CME progressed spatially, and the fitting was stopped when it was clear the lemniscate no longer matched the CME. This may have been due to error in the initial parameter estimation or that the shape of the CMEs evolved over time away from the original fitted lemniscate. Due to the fixed shape of the lemniscate discussed in section 1, the worsening of the fit over time is inevitable.

Figures 3a–3d show the corresponding latitude, longitude, half angle, and radial velocity measurements from using CAT and CAT-HI. The color of the markers corresponds to the event number, which can be found to the left of Figure 3e. The black dashed line shows the line of equivalence. These data are also summarized in Table 1.

The longitude, latitude, and half angle were all consistent between the two tools. The longitude appears to be the most consistent parameter, but this is just an effect of the greater ranges on the axes. Any variation between the tools is due to uncertainty in fitting the lemniscate visually. It may also be the case that a different pair of images were used when performing the fits with CAT and CAT-HI. The radial velocity was higher when measured by CAT-HI for low velocity CMEs, but this disparity is small. Figure 3e shows the difference in the Enlil start time for each event derived by the two tools. The start time is when the CME reaches 21.5 solar radii, the inner boundary of the Enlil model. Figure 3e shows that on average (red dashed line), the CME reaches 21.5 solar radii just under 20 min sooner when it is measured by CAT-HI than when

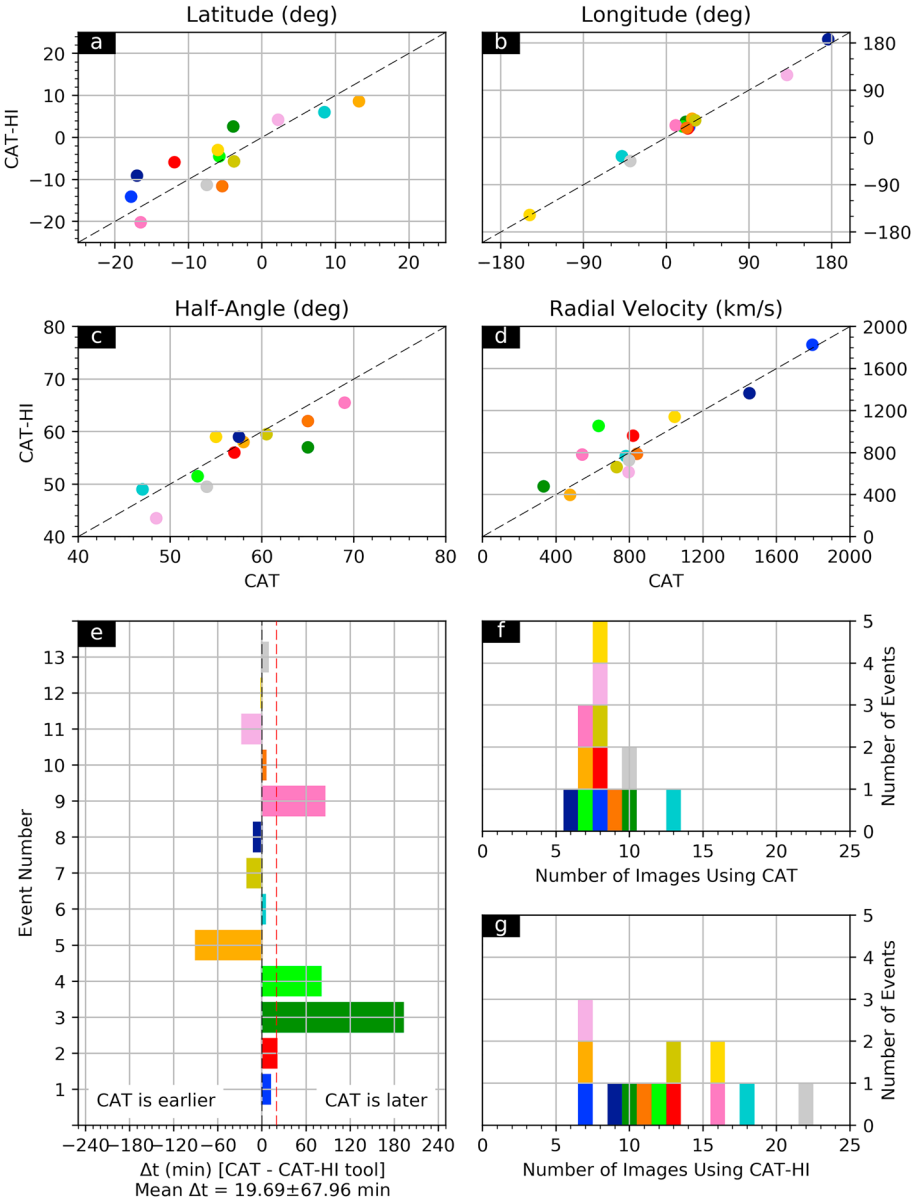

Figure 3. Comparison of corresponding CME metadata for 13 CMEs using the CAT and the CAT-HI. (a) Latitude comparison. (b) Longitude comparison. (c) Half angle comparison. (d) Radial velocity comparison. (e) Relative Enlil initiation time difference between CAT and CAT-HI. (f) and (g) are histograms showing the number of images used to calculate the radial velocity with CAT and CAT-HI, respectively.

it is measured by CAT. However, the standard deviation on this is 69 min, so this difference is insignificant. All additional imagery used by CAT-HI for these events was HI-1, as the events were usually too weak to be seen in HI-2. Note that these images have not been adjusted to account for the spherical projection, the difference being negligible for HI-1 (see appendix). These results show that the inclusion of HI imagery does not make a significant difference to the determination of the CME's radial velocity (at 21.5 solar radii).

Figures 3f and 3g show how many images were used to determine the radial velocity when using the CAT and the CAT-HI, respectively. On average, the operator used ~48% more images when using the CAT-HI. For two events, the operator actually used fewer images when using the CAT-HI than the CAT. These are Events 1 and 11. For some events, the CME was not clearly visible in the heliospheric imagery, and no images were saved. When heliospheric imagery was available, the operator sometimes used fewer images from LASCO C2/C3 and COR2 when using CAT-HI than CAT.

Table 1
Initial Parameters for Coronal Mass Ejections Analyzed in This Study

Enlil start time	Latitude (°)	Longitude (°)	Half angle (°)	Velocity (km/s)	No. images	Event
20160102 01:17	−17.8	25.0	33.5	1,795	8	1
20160102 01:06	−14.1	20.4	27.5	1,826	7	
20160106 18:11	−11.9	23.5	57.0	819	8	2
20160106 17:51	−5.9	17.1	56.0	960	13	
20160221 00:57	−3.9	21.3	65.0	332	10	3
20160220 21:45	2.6	29.6	57.0	478	10	
20160221 17:10	−5.8	18.1	53.0	632	7	4
20160221 15:50	−4.5	20.8	51.5	1,053	12	
20160701 00:03	13.2	28.2	58.0	476	7	5
20160701 01:33	8.6	35.6	58.0	397	7	
20170419 00:28	8.5	−48.2	47.0	780	13	6
20170419 00:24	6.0	−35.9	49.0	766	18	
20170714 06:26	−3.8	31.5	60.5	730	8	7
20170714 06:46	−5.7	32.6	59.5	661	13	
20170723 07:03	−17.0	176.3	57.5	1,452	6	8
20170723 07:14	−9.1	−173.2	59.0	1,365	9	
20170905 02:42	−16.5	10.3	69.0	542	7	9
20170905 01:17	−20.2	22.9	65.5	781	16	
20170906 16:40	−5.4	22.2	65.0	840	9	10
20170906 16:35	−11.6	18.2	62.0	788	11	
20170910 03:10	2.2	131.4	48.5	795	8	11
20170910 03:37	4.2	118.9	43.5	614	7	
20170917 15:23	−6.0	−148.6	55.0	1,045	8	12
20170917 15:24	−3.0	−147.7	59.0	1,140	16	
20171018 12:09	−7.5	−39.2	54.0	797	10	13
20171018 12:01	−11.3	−45.0	49.5	726	22	

Note. For each coronal mass ejection (CME), the first entry (blue text) shows results from CME Analysis Tool, and the second entry (red text) shows results from CME Analysis Tool with Heliospheric Imagery. The final column gives the event numbers and colors for each event.

For each image that is used in determining the radial velocity of a CME, the leading edge radius defined by the lemniscate and the universal time of the image is recorded. Figure 4 shows the evolution of the leading edge of the CME in time, when using CAT and CAT-HI. In order to compare the different events, the *x* axis shows the time relative to the Enlil start time for that event. The Enlil start time is also the time of the WSA map used for the simulation. The top plot shows the leading edge position for the different images when using CAT and the bottom for CAT-HI. Each triangle represents an image. Straight lines have not been fitted to these data as we did not want to make the assumption that the velocity was constant.

The bottom plot shows an increase in images taken after the Enlil start time. This increase is due to the use of HI-1 imagery. The operator was able to identify the leading edge of the CME in HI-1 data to over 60 solar radii in one case, but consistently above 40 solar radii. Above these distances, the leading edge of the CME was too ambiguous and difficult to fit with the lemniscate. Note that the same image used by both tools will have different relative times so will appear in different places on the *x* axis.

Consistent measurement of the leading edge beyond 21.5 solar radii (the inner Enlil boundary) was not possible with CAT due to the limited field of view of the telescopes employed. Figure 4 illustrates the advantage of incorporating HI imagery into CAT; it allows the CME to be tracked to much greater distances from the Sun. It opens up the possibility of verifying the Enlil runs used to estimate the time of arrival of CMEs at Earth and other planets. This is discussed further in section 4.

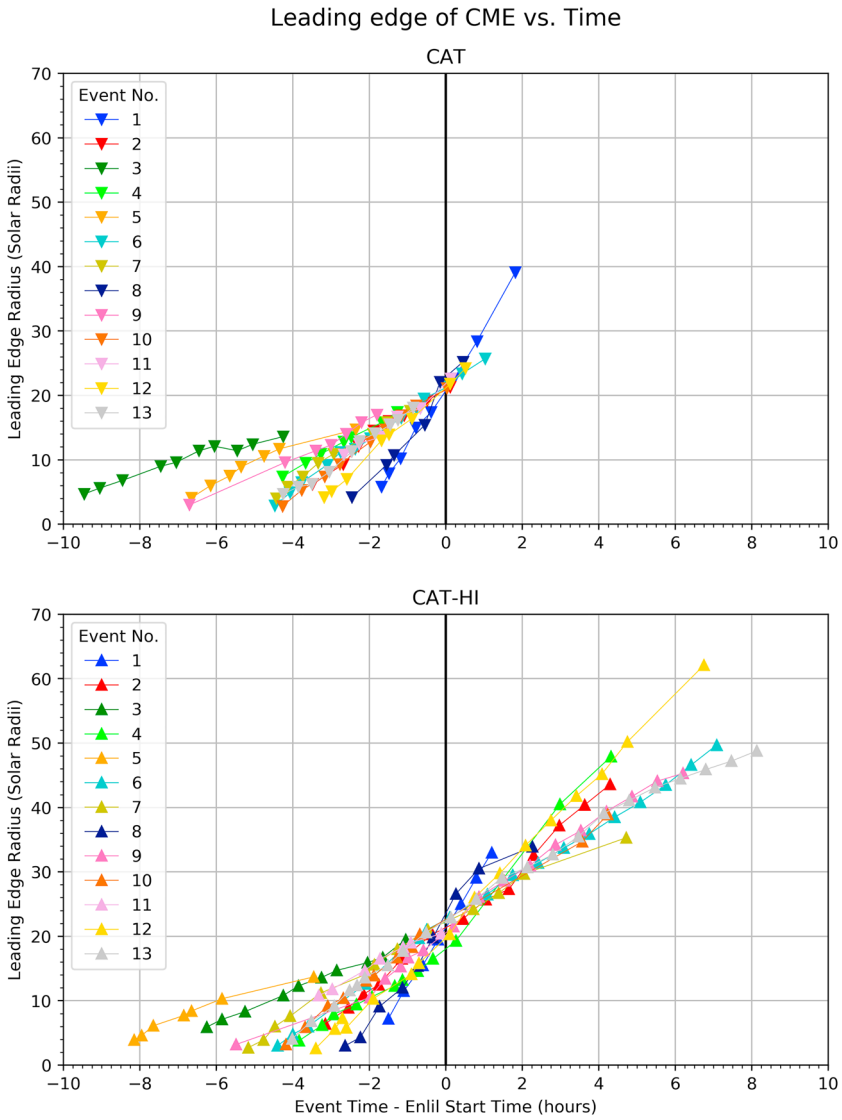

Figure 4. Leading edge radius of CME as a function of time relative to the Enlil start time. Each color shows a different CME. Top shows results for CAT, and bottom shows results for CAT-HI. The inclusion of HI-1 imagery in the latter allows fitting of a CME's leading edge further away from the Sun.

From visual inspection, it is difficult to determine whether any of the CMEs are accelerating or decelerating. Therefore, we fitted a quadratic function (equation (1)) to the profiles in Figure 4 and performed a statistical t test. x is the leading edge of the CME in solar radii, and t is the event time minus the Enlil start time in hours, as shown in Figure 4. The constants a, b, and c represent the acceleration, linear velocity, and position of the leading edge at the Enlil start time, respectively.

$$x = at^2 + bt + c. \tag{1}$$

Equation (1) was fitted to each profile using the method of least squares and the best fit values of a, b, and c, and their respective standard deviations σ_a, σ_b, and σ_c were calculated. This was done with the Python Scipy library. The t statistic was then calculated for the acceleration (and the other parameters) and the degrees of freedom found as the number of images minus 3, for the three parameters. The two-tailed p value could then be calculated. The significance level was set at 5%. Any values of p less than 5% were considered significant, and the CME was considered to be accelerating or decelerating.

These data are summarized in Table 2 for the acceleration parameter. Results for CAT are shown in blue, and those for CAT-HI shown in red, just as in Table 1. Events with a significant p value are shown in bold.

Table 2
Results of Statistical Test for Acceleration/Deceleration

Enlil start time	a (R_S/hr^2)	σ_a (R_S/hr^2)	t	DOF	p (%)	Event
20160102 01:17	0.298	0.182	1.633	5	16.3	1
20160102 01:06	0.155	0.152	1.019	4	36.6	
20160106 18:11	−0.375	0.150	2.490	5	5.52	2
20160106 17:51	**0.115**	**0.051**	**2.241**	**10**	**4.89**	
20160221 00:57	**−0.180**	**0.063**	**2.867**	**7**	**2.41**	3
20160220 21:45	−0.001	0.057	0.009	7	99.3	
20160221 17:10	−0.059	0.057	1.034	4	36.0	4
20160221 15:50	**0.408**	**0.055**	**7.356**	**9**	**4.30×10^{-3}**	
20160701 00:03	**−0.402**	**0.038**	**10.689**	**4**	**4.34×10^{-2}**	5
20160701 01:33	**−0.270**	**0.047**	**5.802**	**4**	**4.39×10^{-1}**	
20170419 00:28	−0.020	0.043	0.450	10	66.2	6
20170419 00:24	**−0.050**	**0.014**	**3.655**	**15**	**2.35×10^{-1}**	
20170714 06:26	**−0.306**	**0.104**	**2.940**	**5**	**3.22**	7
20170714 06:46	**−0.101**	**0.019**	**5.405**	**10**	**2.99×10^{-2}**	
20170723 07:03	0.844	0.673	1.255	3	29.8	8
20170723 07:14	−0.494	0.300	1.647	6	15.1	
20170905 02:42	0.167	0.064	2.604	4	5.98	9
20170905 01:17	0.056	0.035	1.594	13	13.5	
20170906 16:40	−0.059	0.067	0.875	6	41.5	10
20170906 16:35	**−0.091**	**0.031**	**2.928**	**8**	**1.91**	
20170910 03:10	0.340	0.268	1.267	5	26.1	11
20170910 03:37	−0.320	0.118	2.720	4	5.30	
20170917 15:23	−0.124	0.108	1.147	5	30.3	12
20170917 15:24	**0.068**	**0.028**	**2.405**	**13**	**3.18**	
20171018 12:09	0.161	0.178	0.903	7	39.7	13
20171018 12:01	**−0.116**	**0.010**	**12.194**	**19**	**1.98×10^{-8}**	

Note. For each coronal mass ejection (CME), the first entry (blue text) shows results from CME Analysis Tool, and the second entry (red text) shows results from CME Analysis Tool with Heliospheric Imagery. The significance level is set at 5%. Events with a significant p value are in bold. The final column gives the event numbers and colors for each event. DOF = degrees of freedom.

For analysis with CAT, Events 3, 5, and 7 showed a significant acceleration (or deceleration), whereas for CAT-HI, there were eight events (Events 2, 4, 5, 6, 7, 10, 12, and 13). Of the significant CAT results, all three CMEs were decelerating; this was more mixed for the larger sample of significant CAT-HI results, where three CMEs were accelerating and five were decelerating. Note that of the three significant events found with CAT, only two of those were also identified as significant with CAT-HI.

These results suggest that including HI-1 images typically increases the chance of measuring a significant acceleration for the CME compared to just using coronagraph imagery. Interestingly however, the CMEs with a significant acceleration in this sample do not show a consistent behavior, with a few accelerating and the others decelerating. However, the sample size here is small, so we did not attempt further analysis and note that over the radial distances considered, there does not seem to be a universal tendency.

The increased significance of the acceleration estimates achieved via the addition of HI-1 data to CAT-HI does open the possibility of providing the acceleration of a CME to the forecaster as a secondary data product. In principle, this information could be entered into the WSA-Enlil solar wind model and be used to improve the time of arrival predictions of the CME at Earth. However, the other limitations of the tool, primarily the accuracy in fitting the lemniscate visually, result in a lot of uncertainty on the leading edge estimates. This uncertainty affects the acceleration values. We can see that the relative error (σ_a/a) in Table 2 for some events can be greater than 100% (e.g., Event 10 for CAT). As the acceleration is not always a reliable parameter, we

Table 3
Contingency Table Showing Predictions Versus Observations for Each Event

CAT	Forecast hit	Forecast miss
Observed hit	6, 7, 9, 10, 11	13
Observed miss	1, 2, 3, 4, 5,	8, 12
CAT-HI	Forecast hit	Forecast miss
Observed hit	6, 7, 9, 10, 11, 13	—
Observed miss	1, 2, 3, 4, 5	8, 12

*Note.*Top table shows predictions with CME Analysis Tool (CAT) and bottom table for CME Analysis Tool with Heliospheric Imagery (CAT-HI).

judge that the benefit of including it will likely be marginal in an operational context. This view takes into account the added complexity the occasional inclusion (contingent on significance) of an additional free parameter adds to the forecaster's tasks. Given this, we judge it more prudent to retain the current constant velocity paradigm for specification of the initial CME velocity in the WSA-Enlil-cone approach.

3. CME Time of Arrival Predictions With CAT-HI

For each of the 13 CME events, a "cone file" was made using both CAT and CAT-HI, so that WSA-Enlil runs could be performed for each tool and all CMEs. There were two instances where the CMEs were emitted in very close succession, those being two CMEs in mid-February 2016 (Events 3 and 4) and early September 2017 (Events 9 and 10). These "double" CME events were combined into single cone files. This gave 22 WSA-Enlil runs, or 11 events. The model's predicted measurements expected at L1 could then be compared to data from the Deep Space Climate Observatory (https://www.nesdis.noaa.gov/content/dscovr-deep-space-climate-observatory).

Table 3 shows the predictions and outcomes for the 13 CMEs with regard to hitting L1. The contingency tables show prediction results using CAT and CAT-HI. The results for both tools are similar. The tables are defined very simply, as they are intended only as a simple heuristic of whether CAT-HI yields very different results from CAT. CMEs are recorded as observed at L1 by Enlil if there is a peak in the cloud tracer parameter (Odstrčil & Pizzo, 2009). Similarly, CMEs are recorded as observed at Earth in L1 observations if there is an observed shock arrival time entry in the CCMC CME scoreboard (https://kauai.ccmc.gsfc.nasa.gov/CMEscoreboard/PreviousPredictions/), for entries where the CCMC CME start time at 21.5 solar radii is consistent with ours. Hits are then defined as times when CMEs are observed in Enlil and in L1 data, and so forth. Under this definition, the preliminary indications are that there is little difference between the two tools: Seven CMEs were predicted correctly for CAT, and eight for CAT-HI. For both tools, there were five false alarms.

Note these results should not be overinterpreted, as the definitions used are very simple. Specifically, we do not define a threshold for the peak in the cloud tracer parameter—peak values can range from 10^{1} to 10^{-30}, where the latter are likely to be associated with "glancing blows." We have not introduced a threshold here—the presence of a peak of any magnitude is simply considered as "observed in Enlil." Likewise, we have not defined a minimum threshold for the time error (between an observation of a CME in Enlil and L1 data) required to constitute a hit. Differences can be greater than a day.

Three of the CMEs predicted to hit are presented in Figure 5. Figure 5a shows the single CME event from July 2017 (Event 7), and Figure 5b shows the double CME event from September 2017 (Events 9/10), the same event discussed by Redmon et al. (2018). For Figures 5a and 5b, the top, middle, and bottom panels show magnetic field magnitude, solar wind velocity, and solar wind density, respectively. Blue lines show predictions when using CME parameters derived with CAT, red lines when using CAT-HI, and green shows data from Deep Space Climate Observatory. Vertical dashed lines show the Enlil start time.

For both of these events, the predicted time of arrival was late on both the CAT and CAT-HI runs. The double-headed arrows in Figure 5 describe the range of predictions made by other people from the CME scoreboard. In Figure 5a, our prediction is on the late end of this range. For Figure 5b, we have predicted both CMEs to be later than the range of predictions from the CME scoreboard. Wold et al. (2018) performed

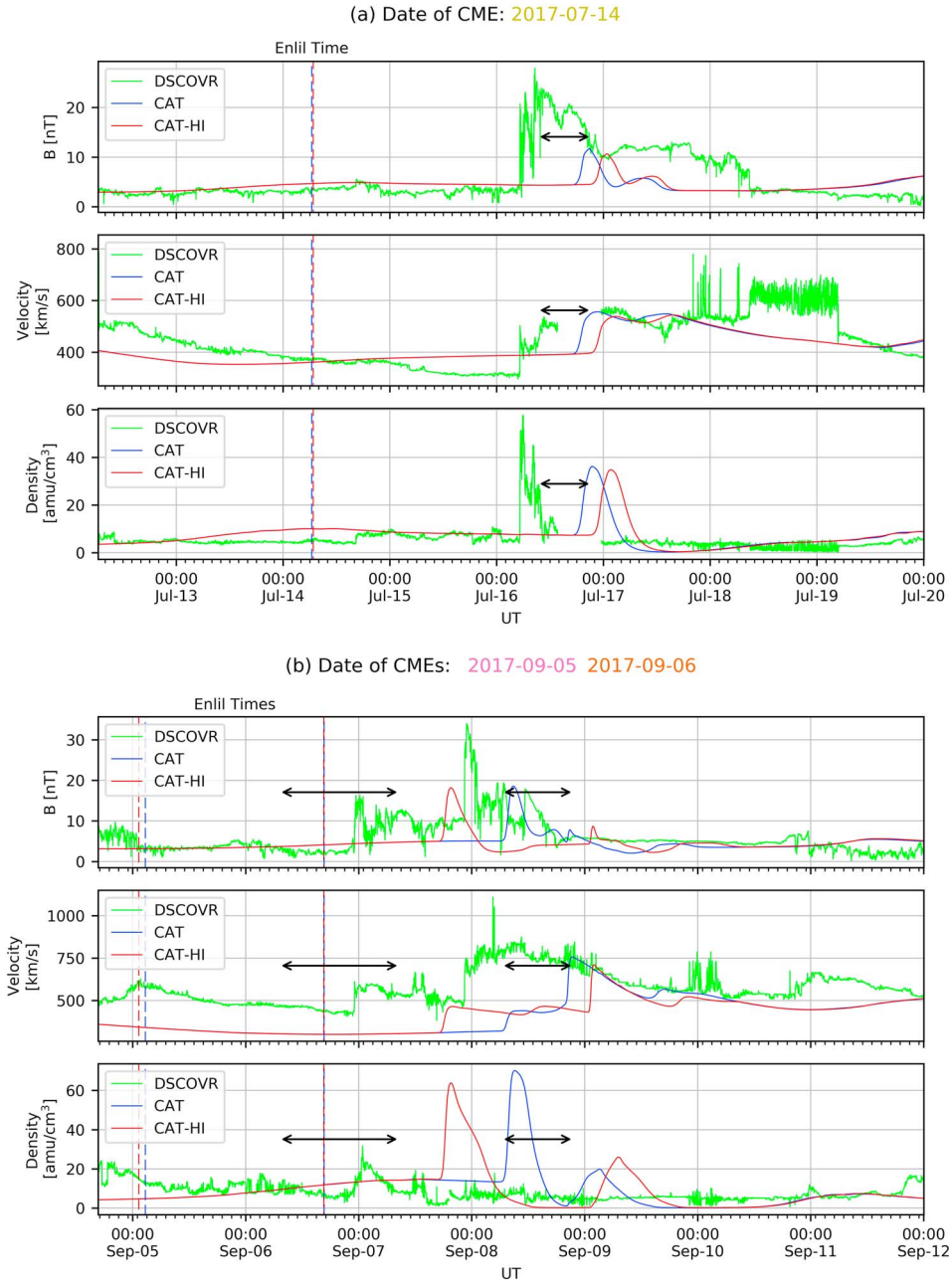

Figure 5. WSA-Enlil time of arrival prediction of the CME compared to Deep Space Climate Observatory data for CMEs in (a) July 2017 (Event 8) and (b) September 2017 (Events 9/10). For (a) and (b), respectively, top: magnetic field magnitude. Middle: solar wind velocity. Bottom: solar wind density. Double-headed arrows show the range of predictions on the CME scoreboard (see text).

studies with a large number of CMEs and found on average, the WSA-Enlil prediction is 4 hr early. A study by Möstl et al. (2014; not using WSA-Enlil) found a similar result, and this was attributed to an overestimation of the CME speed. The CMEs analyzed in Figure 5 arrived earlier than predicted, opposite to the findings of Möstl et al. (2014) and Wold et al. (2018). Figure 5a shows that the CAT run was closer to the actual arrival time than CAT-HI, whereas in Figure 5b, the CAT-HI run performed better but was still nearly 24 hr late. For the double CME event, interaction between the CMEs may have complicated their motion, making predicting the time of arrival more difficult in this case.

Consequently, the preliminary indications of this study (with small sample size and without rigorous thresholds) are that incorporating the HI imagery into CAT to further constrain the CME parameters introduced

at the Enlil inner boundary does not produce any meaningful improvement in the resulting estimated time of arrival of CMEs using Enlil. This is similar to the results of Barnard et al. (2017). They used HI data and a drag-based model to estimate the time of arrival of CMEs but found that the HI data did not improve the predictions compared to the SWPC prediction.

However, the advantages of using the HI imagery may be in using it to update initial predictions and to prune ensemble forecasts. This is discussed in section 4.

4. Discussion

Accurate determination of the time of arrival of CMEs at Earth has so far proven difficult. For example, Millward et al. (2013) found, with all three spacecraft, an average absolute error in the arrival time of 7.5 hr when using the CAT to give input values to the WSA-Enlil model. It is worth noting that determining CMEs parameters with CAT-HI is partly subjective due to CMEs not having a well-defined edge or geometry. A different user of CAT-HI, such as an experienced forecaster, would get slightly different values for the CME parameters. However, we expect that the overall results would agree with the conclusions of this study (that there are no significant differences between the two tools). Due to the easier availability of data, this study only looked at CMEs from January 2016 to October 2017 and was considered sufficient for this proof-of-concept study. Any future study should also use data from a wider range of years to reduce the uncertainty in the results and use a more formal testing procedure.

The predicted time of arrival of the CME depends on the initial CME parameters such as its speed (Lee et al., 2013; Mays et al., 2015) and the ambient solar wind conditions throughout the whole heliosphere (Lee et al., 2015; Wold et al., 2018). Möstl et al. (2014) and Wold et al. (2018) have found that on average, the estimated time of arrival is a few hours too early (unlike in Figures 5a and 5b), either because the initial speed of the CME is overestimated or the CME decelerates through the heliosphere. Even for experienced forecasters, determining the CME's initial properties is inevitably uncertain. Observational knowledge of the state of the entire solar wind is also not possible to obtain, and instead, forecasters must rely on models.

In terrestrial weather, ensemble modeling is used to indicate uncertainty in the predictions. Instead of using a single set of initial conditions for one model run, ensemble modeling takes a set of perturbed initial conditions and creates a set of runs (an ensemble), which describes the uncertainty in the initial conditions. The spread of the ensemble can be used to assign a probability to a particular outcome. Ensemble modeling can be used to improve the forecasting of chaotic systems, such as hurricanes (e.g., Zhang & Krishnamurti, 1997), and to generate seasonal forecasts (e.g., Arribas et al., 2011; MacLachlan et al., 2015).

In recent years, it has become increasingly clear that ensemble modeling could also improve space weather forecasting (Henley & Pope, 2017; Murray, 2018; Riley et al., 2013). Many studies have been conducted applying ensemble modeling to CME forecasting (e.g., Amerstorfer et al., 2018; Cash et al., 2015; Emmons et al., 2013; Lee et al., 2013; Lee et al., 2015), including Mays et al. (2015) who applied ensemble modeling to an operational system. Amerstorfer et al. (2018) have also applied ensemble modeling to HI observations of CMEs. In general, it has been found that ensemble modeling of CMEs reduces the error in the time of arrival and usually includes the correct prediction in its range. Applying ensemble methods to CME propagation requires consideration of the underlying dynamics, as this affects the approach used to set up the ensemble. Pizzo et al. (2015) show that CME shock front propagation may be treated more as a deterministic issue (dominated by unknown initial conditions, similar to tsunami propagation), rather than as a chaotic problem (dominated by internal variability, similar to hurricane propagation).

CAT-HI gives the opportunity to improve model predictions by two routes: pruning away unlikely ensemble members and providing mid-trajectory corrections, both using the HI data. When operators make a prediction using imagery from the LASCO and COR2 coronagraphs, they are unable to track the CME after it passes beyond LASCO C3's field of view. With CAT-HI, the STEREO HI data are incorporated into the operational tool, yielding data for a longer period after the Enlil start time (see Figure 4). Therefore, with postprocessing of the WSA-Enlil model results to generate synthetic white light images (Odstrčil & Pizzo, 2009), it should be possible to compare the original WSA-Enlil runs with the latest HI imagery. The ensemble runs could then be pruned so that the ensemble spread better reflects the true uncertainty, or the model rerun with the new information, providing trajectory corrections for CMEs. This process could be repeated every few hours as new HI data became available, allowing the forecasters to increase the accuracy of their

predictions over time, albeit with decreasing forecast lead time. This would be a major step forwards in predicting CME arrival times. It would also be beneficial if the WSA-Enlil model could be rerun with the Enlil inner boundary at a greater distance from the Sun, but currently, this is not possible.

STEREO A is in a continuously drifting orbit relative to the Earth and is currently approaching the Earth. As the angle between the Sun-Earth and Sun-STEREO A lines decreases from −90° toward 0° , the accuracy of determining the CME's initial parameters is expected to worsen. For this study, STEREO A was located between Earth ecliptic longitudes of −164° and −128°, which is nonideal. Many authors have recently lobbied for a permanent mission at the L4 or L5 Lagrange points to counter for this loss of capability and to ensure good-quality and long-term space weather monitoring capabilities (Amerstorfer et al., 2018; Hapgood, 2017; Wold et al., 2018). CAT-HI could easily be adapted to use imagery from dedicated operational missions at L1 and L4/L5. It would be particularly powerful if a mission at L4/L5 had a heliospheric imager onboard. With the added HI, this would give continuous observation of CMEs from permanent viewing points and improve the quality of space weather monitoring. This study has used science-grade data, as its improved quality allows easier identification of CMEs further out than is possible with beacon-grade data, potentially improving the information available to forecasters. However, while we have shown CAT-HI can use beacon-quality data, we have not investigated performance with this so cannot state what the benefit is (if any) of science-quality data over beacon quality. Further work would be required to assess this and may help to inform downlink requirements for an operational mission.

5. Summary

This paper has introduced an adapted version of the operational CAT. CAT-HI incorporates heliospheric imagery (HI) from the STEREO spacecraft and hence provides the possibility of tracking CMEs out to much greater distances than was possible with CAT. Although the use of HI imagery does not produce an improvement in the initial prediction of a CME's arrival time, it could potentially be used in conjunction with ensemble modeling. Once a WSA-Enlil prediction is made, the model output could be postprocessed to generate synthetic white light imagery. This would allow easy comparison with new HI imagery, as this becomes available, allowing the forecast to be updated by pruning ensemble runs. Any new HI imagery could also be used as the basis for new CME fits to use as input into new model runs, also allowing forecast updates. Therefore, we see this tool not as an improvement to the CAT tool, but as a proof of concept for using HI data operationally. This tool also supports the development of a dedicated L4/L5 operational mission equipped with a heliospheric imager. It is our intention that CAT-HI will enter use operationally at both National Oceanic and Atmospheric Administration/SWPC and MOSWOC.

Appendix A

In this section, we discuss the projection of HI images onto a flat plane, the so-called plane of sky. This is used by the coronagraphs, and it is helpful to apply the same concept to the HI images, so they can be treated equivalently by CAT-HI. Figure A1 shows the viewing geometry of the HI imagers. In CAT-HI, it has been assumed that the image can be displayed as a flat, square image like COR2, which is the red plane in Figure A1. However, the HIs have wide fields of view. Therefore, the correct projection is onto the inside of a sphere, which is the blue plane in Figure A1. This curved image then needs transforming to the plane of sky. In this appendix, we quantify the difference in radial distances under these two projections in order to understand whether a flat projection is justified.

In Figure A1, position O represents the location of STEREO A (or B). S represents the position of the Sun, which for convenience, lies in both the red and blue planes. OA (or OV) is the viewing direction of a HI camera, and OC (or OF) is the direction of the point of interest in the image, the leading edge of the CME. α_c and β_c are the horizontal and vertical angles between the viewing direction and the CME direction. α is the angle between the viewing direction and the Sun, which from Eyles et al. (2009) is 14° for HI-1 and 53.7° for HI-2.

We can use Figure A1 to calculate the distance CS, the "correct" plane of sky projection. This can then be compared to the original determination where the HI image was projected as a flat square. We call the distance $OS = R_S$, the Sun-spacecraft distance. Then $OA = R_S\cos(\alpha)$ and $AS = R_S\sin(\alpha)$. $AB = R_S\cos(\alpha)\tan(\alpha_c)$ so $BS = R_S(\sin(\alpha) - \cos(\alpha)\tan(\alpha_c))$. $AE = R_S\cos(\alpha)\tan(\beta_c)$ and $AE = BC$. Finally, we can get CS_{Circ} using

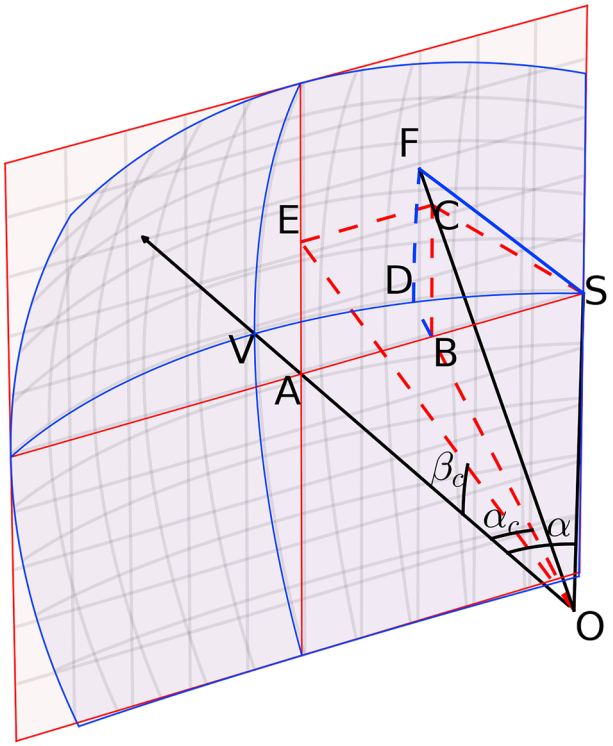

Figure A1. The projection of HI images onto a flat plane (red) and the inside of a sphere (blue). *O* is the location of STEREO A, and *S* is the location of the Sun. *OA*/*OV* is the viewing direction of the HI camera. *OC*/*OF* is the direction of the point of interest, the leading edge of the CME. α_c and β_c are the horizontal and vertical angles from the viewing direction to the CME. α is the angle between the viewing direction and the Sun.

Pythagoras' theorem (equation (A1)), where the subscript *circ* is to distinguish that this difference refers to the correct projection.

$$CS_{Circ} = R_S\sqrt{\cos^2(\alpha)\tan^2(\beta_c) + \left(\sin(\alpha) - \cos(\alpha)\tan(\alpha_c)\right)^2}. \quad \text{(A1)}$$

To compare to CAT-HI, we get the equivalent distance in the coordinates of the flat projection, where the x coordinate is in the α direction and the y coordinate is in the β direction. The equivalent radial distance CS_{Flat} is given by equation (A2).

$$CS_{Flat} = R_S\sqrt{(\alpha - \alpha_c)^2 + \beta_c^2}. \quad \text{(A2)}$$

We now calculate CS_{Circ}/CS_{Flat} for all combinations of α_c and β_c possible in the HI-1 and HI-2 viewing geometries. This is shown in Figure A2. Note that the scales are different for the HI-1 and HI-2 cases.

For HI-1, we can see that the greatest difference between CS_{Circ} and CS_{Flat} is ~1.5%, or 1.015 on the color bar in Figure A2 (left). Typical radial distances of the leading edge of the CME might be of the order 30–50 solar radii (see Figure 4), giving a maximum possible error of less than a solar radii. Given the other assumptions and constraints of CAT-HI, this difference is not significant.

For HI-2, the greatest difference is ~22%, or 1.22 on the color bar in Figure A2 (right). If CAT-HI measures a point at 150 solar radii in the plane of the sky with the flat field assumption, it will overestimate the distance by ~27 solar radii, a significant distance. Hence, assuming that the HI-2 image can be treated as a flat square is a poor assumption and will lead to significant errors when matching the lemniscate to the image. This does not affect the results presented in this paper, as we have not included any matches from HI-2.

We can also observe the distortion by comparing the flat, square assumption with the equivalent image projected onto the inside of a sphere. This is illustrated with "fake" images in Figure A3. The top row shows HI-1 projections, and the bottom row shows HI-2 projections. The left column shows the image plotted as a

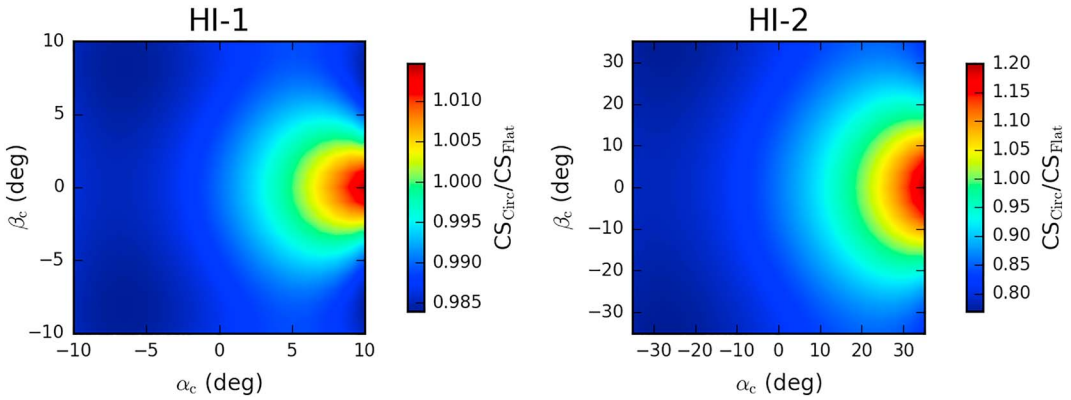

Figure A2. CS_{Circ}/CS_{Flat} for all values of angles α_c and β_c. Left shows HI-1, and right shows HI-2. The Sun is to the right in these subfigures.

flat square while the middle column shows the image plotted onto the inside of a sphere, as it would appear looking along the viewing direction of the telescope. The Sun-Spacecraft distance is set at 215 solar radii and is not assumed to point in a particular direction. The right column shows the position error of any point in the image when projected as a flat square. So in order for the flat image to match the curved image, those pixels that are red need moving radially outwards by this amount. Likewise, blue pixels need moving radially inwards to match the curved image.

Figure A2 shows us that for HI-1, there is very little difference between the correct curved projection (in the middle) and the flat projection (on the left). The right column shows us that assuming a Sun-Spacecraft distance of 215 solar radii, features in the flat projection will be located no more than 0.8 solar radii away from the correct position (in a plane containing the Sun). However, for HI-2, the wider field of view creates a much greater distortion, and toward the corners, the leading edge of the CME can be projected in the wrong place by over 20 solar radii. This is a more significant error.

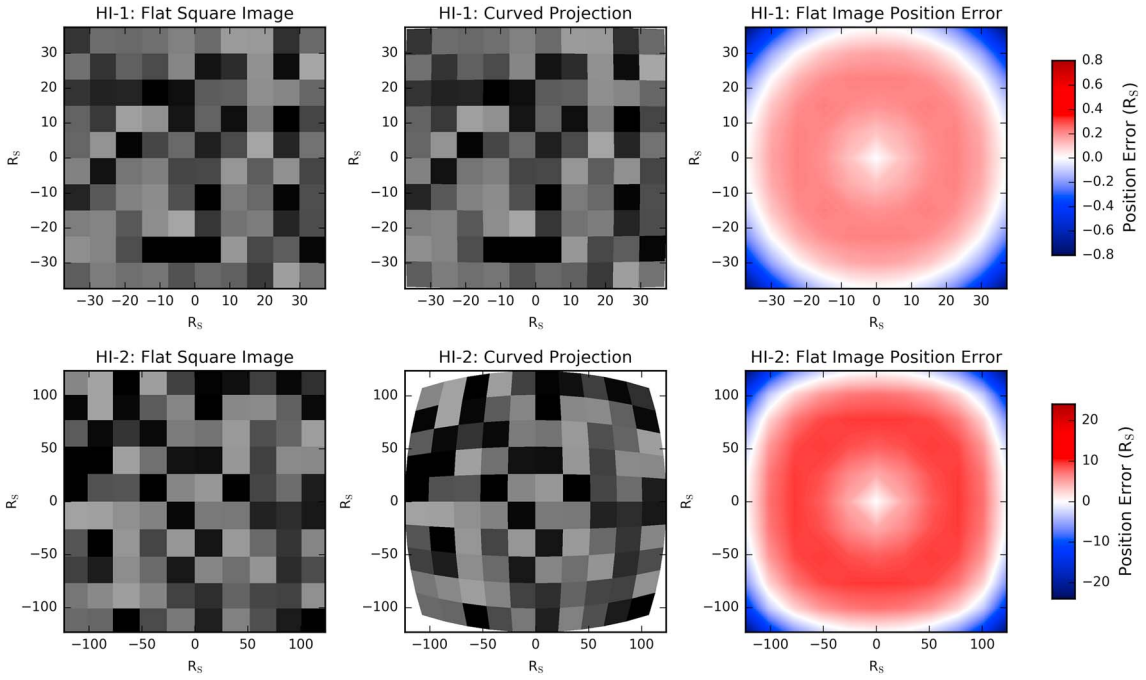

Figure A3. Flat versus curved projections. Top row is HI-1, and bottom row is HI-2. Left column shows an image plotted as a square, and the middle column shows the image plotted onto the inside of a sphere. The right column shows the location error for each point in the image when projected as a flat square. The pointing direction is general and assumes a Sun-Spacecraft distance of 215 solar radii.

This analysis shows us that the curvature of the image makes a negligible difference for the HI-1 images, and so we have used the more convenient flat square projection in CAT-HI. However, the error that comes from this assumption for HI-2 is much greater. For this study, we did not use HI-2 images, so the results are not affected, but these effects should be considered for future studies if it is desired to extend these effects further out.

Acknowledgments
S. J. W. was supported by NERC StudentshipNE/L002493/1. S. J. W. would also like to acknowledge the industrial placement grant provided by the Central England NERC Training Alliance (CENTA) that enabled the work to be undertaken at the Met Office. Imagery for SOHO and STEREO can be found at the U.K. Solar System Data Centre (https://www.ukssdc.ac.uk/solar/). DSCOVR data can be found online (https://www.ngdc.noaa.gov/dscovr/portal/#/). We would also like to thank V. Pizzo and two anonymous reveiwers for their very helpful suggestions in revising this paper.

References

Amerstorfer, T., Móstl, C., Hess, P., Temmer, M., Mays, M. L., Reiss, M. A., et al. (2018). Ensemble prediction of a halo coronal mass ejection using heliospheric imagers. *Space Weather*, *16*, 784–801. https://doi.org/10.1029/2017SW001786

Arge, C., Luhmann, J., Odstrčil, D., Schrijver, C., & Li, Y. (2004). Stream structure and coronal sources of the solar wind during the May 12th, 1997 CME. *Journal of Atmospheric and Solar-Terrestrial Physics*, *66*(15), 1295–1309. https://doi.org/https://doi.org/10.1016/j.jastp.2004.03.018, towards an Integrated Model of the Space Weather System.

Arge, C. N., Odstrčil, D., Pizzo, V. J., & Mayer, L. R. (2003). Improved method for specifying solar wind speed near the Sun. *AIP Conference Proceedings*, *679*(1), 190–193. https://doi.org/10.1063/1.1618574

Arge, C. N., & Pizzo, V. J. (2000). Improvement in the prediction of solar wind conditions using near-real time solar magnetic field updates. *Journal of Geophysical Research*, *105*(A5), 10,465–10,479. https://doi.org/10.1029/1999JA000262

Arribas, A., Glover, M., Maidens, A., Peterson, K., Gordon, M., MacLachlan, C., et al. (2011). The GloSea4 ensemble prediction system for seasonal forecasting. *Monthly Weather Review*, *139*(6), 1891–1910. https://doi.org/10.1175/2010MWR3615.1

Barnard, L. A., Koning, C. A., Scott, C. J., Owens, M. J., Wilkinson, J., & Davies, J. A. (2017). Testing the current paradigm for space weather prediction with heliospheric imagers. *Space Weather*, *15*, 782–803. https://doi.org/10.1002/2017SW001609

Brueckner, G. E., Howard, R. A., Koomen, M. J., Korendyke, C. M., Michels, D. J., Moses, J. D., et al. (1995). The Large Angle Spectroscopic Coronagraph (LASCO). *Solar Physics*, *162*(1), 357–402. https://doi.org/10.1007/BF00733434

Cash, M. D., Biesecker, D. A., Pizzo, V., Koning, C. A., Millward, G., Arge, C. N., et al. (2015). Ensemble modeling of the 23 july 2012 coronal mass ejection. *Space Weather*, *13*, 611–625. https://doi.org/10.1002/2015SW001232

Colaninno, R. C., Vourlidas, A., & Wu, C. C. (2013). Quantitative comparison of methods for predicting the arrival of coronal mass ejections at Earth based on multiview imaging. *Journal of Geophysical Research: Space Physics*, *118*, 6866–6879. https://doi.org/10.1002/2013JA019205

de Koning, C. A., Millward, G., Pizzo, V. J., & Biesecker, D. A. (2012). *Problems encountered when characterizing CMEs in an operational setting, in: Space Weather: The Space Radiation Environment* (Proc. 11th Ann. Intl). *Edited by* Q. Hu, G. Li, G. P. Zank, G. Fry, X. Ao, & J. Adams. CA: Astrophys Conf., AIP,Palm Springs.

Domingo, V., Fleck, B., & Poland, A. I. (1995). The SOHO mission: An overview. *Solar Physics*, *162*(1), 1–37. https://doi.org/10.1007/BF00733425

Driesman, A., Hynes, S., & Cancro, G. (2008). The STEREO observatory. *Space Science Reviews*, *136*(1), 17–44. https://doi.org/10.1007/s11214-007-9286-z

Emmons, D., Acebal, A., Pulkkinen, A., Taktakishvili, A., MacNeice, P., & Odstrčil, D. (2013). Ensemble forecasting of coronal mass ejections using the WSA-ENLIL with CONED Model. *Space Weather*, *11*, 95–106. https://doi.org/10.1002/swe.20019

Eyles, C. J., Harrison, R. A., Davis, C. J., Waltham, N. R., Shaughnessy, B. M., Mapson-Menard, H. C. A., et al. (2009). The heliospheric imagers onboard the STEREO mission. *Solar Physics*, *254*(2), 387–445. https://doi.org/10.1007/s11207-008-9299-0

Hapgood, M. (2017). L1L5Together: Report of workshop on future missions to monitor space weather on the Sun and in the solar wind using both the L1 and L5 Lagrange points as valuable viewpoints. *Space Weather*, *15*, 654–657. https://doi.org/10.1002/2017SW001652

Harrison, R. A., Davies, J. A., Biesecker, D., & Gibbs, M. (2017). The application of heliospheric imaging to space weather operations: Lessons learned from published studies. *Space Weather*, *15*, 985–1003. https://doi.org/10.1002/2017SW001633

Henley, E. M., & Pope, E. C. D. (2017). Cost-loss analysis of ensemble solar wind forecasting: Space weather use of terrestrial weather tools. *Space Weather*, *15*, 1562–1566. https://doi.org/10.1002/2017SW001758

Hill, F. (2018). The Global Oscillation Network Group facility—An example of research to operations in space weather. *Space Weather*, *16*, 1488–1497. https://doi.org/10.1029/2018SW002001

Howard, R. A., Moses, J. D., Vourlidas, A., Newmark, J. S., Socker, D. G., Plunkett, S. P., et al. (2008). Sun Earth Connection Coronal and Heliospheric Investigation (SECCHI). *Space Science Reviews*, *136*(1), 67. https://doi.org/10.1007/s11214-008-9341-4

Howard, T. A., & Tappin, S. J. (2010). Application of a new phenomenological coronal mass ejection model to space weather forecasting. *Space Weather*, *8*, S07004. https://doi.org/10.1029/2009SW000531

Kaiser, M. L., Kucera, T. A., Davila, J. M., Cyr, O. C. St., Guhathakurta, M., & Christian, E. (2008). The STEREO mission: An introduction. *Space Science Reviews*, *136*(1), 5–16. https://doi.org/10.1007/s11214-007-9277-0

Lee, C. O., Arge, C. N., Odstrčil, D., Millward, G., Pizzo, V., & Lugaz, N. (2015). Ensemble modeling of successive halo CMEs: A case study. *Solar Physics*, *290*, 1207–1229. https://doi.org/10.1007/s11207-015-0667-2

Lee, C. O., Arge, C. N., Odstrčil, D., Millward, G., Pizzo, V., Quinn, J. M., & Henney, C. J. (2013). Ensemble modeling of CME propagation. *Solar Physics*, *285*, 349–368. https://doi.org/10.1007/s11207-012-9980-1

Lugaz, N. (2010). Accuracy and limitations of fitting and stereoscopic methods to determine the direction of coronal mass ejections from heliospheric imagers observations. *Solar Physics*, *267*, 411–429. https://doi.org/10.1007/s11207-010-9654-9

Lugaz, N., Kintner, P., Möstl, C., Jian, L. K., Davis, C. J., & Farrugia, C. J. (2012). Heliospheric observations of STEREO-directed coronal mass ejections in 2008–2010: Lessons for future observations of Earth-directed CMEs. *Solar Physics*, *279*, 497–515. https://doi.org/10.1007/s11207-012-0007-8

Móstl, C., Amla, K., Hall, J. R., Liewer, P. C., Jong, E. M. D., Colaninno, R. C., et al. (2014). Connecting speeds, directions and arrival times of 22 coronal mass ejections from the Sun to 1 AU. *Astronomy Journal*, *787*(2), 119. https://doi.org/10.1088/0004-637X/787/2/119

MacLachlan, C., Arribas, A., Peterson, K. A., Maidens, A., Fereday, D., Scaife, A. A., et al. (2015). Global Seasonal forecast system version 5 (GloSea5): A high-resolution seasonal forecast system. *Quarterly Journal of the Royal Meteorological Society*, *141*(689), 1072–1084. https://doi.org/10.1002/qj.2396

Mays, M. L., Taktakishvili, A., Pulkkinen, A., MacNeice, P. J., Rastätter, L., Odstrčil, D., et al. (2015). Ensemble modeling of CMEs using the WSA–ENLIL+ Cone model. *Solar Physics*, *290*(6), 1775–1814. https://doi.org/10.1007/s11207-015-0692-1

Millward, G., Biesecker, D., Pizzo, V., & Koning, C. A. (2013). An operational software tool for the analysis of coronagraph images: Determining CME parameters for input into the WSA-Enlil heliospheric model. *Space Weather*, *11*, 57–68. https://doi.org/10.1002/swe.20024

Murray, S. A. (2018). The importance of ensemble techniques for operational space weather forecasting. *Space Weather*, *16*, 777–783. https://doi.org/10.1029/2018SW001861

Odstrčil, D., & Pizzo, V. J. (1999). Distortion of the interplanetary magnetic field by three-dimensional propagation of coronal mass ejections in a structured solar wind. *Journal of Geophysical Research*, *104*(A12), 28,225–28,239. https://doi.org/10.1029/1999JA900319

Odstrčil, D. (2003). Modeling 3-D solar wind structure. *Advances in Space Research*, *32*(4), 497–506. https://doi.org/https://doi.org/10.1016/S0273-1177(03)00332-6

Odstrčil, D., Linker, J. A., Lionello, R., Mikic, Z., Riley, P., Pizzo, V. J., & Luhmann, J. G. (2002). Merging of coronal and heliospheric numerical two-dimensional MHD models. *Journal of Geophysical Research*, *107*(A12), 1493. https://doi.org/10.1029/2002JA009334

Odstrčil, D., & Pizzo, V. J. (2009). Numerical heliospheric simulations as assisting tool for interpretation of observations by STEREO heliospheric imagers. *Solar Physics*, *259*(1), 297–309. https://doi.org/10.1007/s11207-009-9449-z

Parsons, A., Biesecker, D., Odstrčil, D., Millward, G., Hill, S., & Pizzo, V. (2011). Wang-Sheeley-Arge-Enlil Cone model transitions to operations. *Space Weather*, *9*, 03004. https://doi.org/10.1029/2011SW000663

Pizzo, V. J., Koning, C., Cash, M., Millward, G., Biesecker, D. A., Puga, L., et al. (2015). Theoretical basis for operational ensemble forecasting of coronal mass ejections. *Space Weather*, *13*, 676–697. https://doi.org/10.1002/2015SW001221

Pulkkinen, A., Bernabeu, E., Thomson, A., Viljanen, A., Pirjola, R., Boteler, D., et al. (2017). Geomagnetically induced currents: Science, engineering, and applications readiness. *Space Weather*, *15*, 828–856. https://doi.org/10.1002/2016SW001501

Redmon, R. J., Seaton, D. B., Steenburgh, R., He, J., & Rodriguez, J. V. (2018). September 2017's geoeffective space weather and impacts to Caribbean radio communications during hurricane response. *Space Weather*, *16*, 1190–1201. https://doi.org/10.1029/2018SW001897

Riley, P., Linker, J. A., & Mikic, Z. (2013). On the application of ensemble modeling techniques to improve ambient solar wind models. *Journal of Geophysical Research: Space*, *118*, 600–607. https://doi.org/10.1002/jgra.50156

Rouillard, A. P., Davies, J. A., Forsyth, R. J., Rees, A., Davis, C. J., Harrison, R. A., et al. (2008). First imaging of corotating interaction regions using the STEREO spacecraft. *Geophysical Research Letters*, *35*, L10110. https://doi.org/10.1029/2008GL033767

Sheeley, Jr. N. R. (2017). Origin of the Wang–Sheeley–Arge solar wind model. *History of Geo- and Space Sciences*, *8*(1), 21–28. https://doi.org/10.5194/hgss-8-21-2017

Sibley, A., Biesecker, D., Millward, G., & Gibbs, M. (2012). Space weather, impacts and forecasting: an overview. *Weather*, *67*(5), 115–120. https://doi.org/10.1002/wea.1915

Wang, Y.-M., & Sheeley, N. R. Jr. (1990). Solar wind speed and coronal flux-tube expansion. *Astrophysical Journal*, *355*, 726–732. https://doi.org/10.1086/168805

Wold, A. M., Mays, M. L., Taktakishvili, A., Jian, L. K., Odstrcil, D., & MacNeice, P. (2018). Verification of real-time WSA-ENLIL+ Cone simulations of CME arrival-time at the CCMC from 2010 to 2016. *Journal of Space Weather and Space Climate*, *8*, A17. https://doi.org/10.1051/swsc/2018005

Xie, H., Ofman, L., & Lawrence, G. (2004). Cone model for halo CMEs: Application to space weather forecasting. *Journal of Geophysical Research*, *109*, A03109. https://doi.org/10.1029/2003JA010226

Zhang, Z., & Krishnamurti, T. N. (1997). Ensemble forecasting of hurricane tracks. *Bulletin of the American Meteorological Society*, *78*(12), 2785–2796. https://doi.org/10.1175/1520-0477(1997)078<2785:EFOHT>2.0.CO;2